



Full length article

A Strategy to Enhance the B-Solubility and Mechanical Properties of Ti–B–N Thin Films

Rebecca Janknecht^a, Rainer Hahn^b, Nikola Koutná^{a,c}, Tomasz Wójcik^a, Eleni Ntemou^d,
Andreas Steiger-Thirsfeld^e, Zhuo Chen^f, Alexander Kirnbauer^a, Peter Polcik^g,
Szilárd Kolozsvári^g, Zaoli Zhang^f, Daniel Primetzhofe^d, Paul H. Mayrhofer^a

^a Institute of Materials Science and Technology, TU Wien, Austria^b Christian Doppler Laboratory for Surface Engineering of high-performance Components, TU Wien, Austria^c Department of Physics, Chemistry, and Biology (IFM), Linköping University, Sweden^d Department of Physics and Astronomy, Uppsala University, Sweden^e University Service Facility for Transmission Electron Microscopy (USTEM), TU Wien, Austria^f Erich Schmid Institute of Materials Science, Austrian Academy of Sciences, Austria^g Plansee Composite Materials GmbH, Germany

ARTICLE INFO

Keywords:

Physical vapor deposition (PVD)

Solubility

Fracture toughness

Mechanical properties

DFT

ABSTRACT

The Ti–B–N system offers a wide range of possible meta(stable) phases, making it interesting for science and industry. However, the solubility for B within the face-centered cubic (fcc)-TiN lattice is rather limited and less studied, especially without forming B-rich phases. Therefore, we address how chemistries along the TiN–TiB₂ or TiN–TiB tie-line influence this B-solubility. The variation between these two tie-lines is realized through non-reactive co-sputtering of a TiN, TiB₂, and Ti target. We show that for variations along the TiN–TiB tie-line, even 8.9 at.% B (equivalent to 19.3 at.% non-metal fractions) can fully be incorporated into the fcc-TiN_y lattice without forming other B-containing phases. The combination of detailed microstructural characterization through X-ray diffraction and transmission electron microscopy with ab initio calculations of fcc-Ti_{1-x}N_x, fcc-TiN_{1-x}B_x, and fcc-TiN_{1-2x}B_x solid solutions indicates that B essentially substitutes N.

The single-phase fcc-TiB_{0.17}N_{0.69} (the highest B-containing sample along the TiN–TiB tie-line studied) exhibits the highest hardness H of 37.1 ± 1.9 GPa combined with the highest fracture toughness K_{IC} of 3.0 ± 0.2 MPa·m^{1/2} among the samples studied. These are markedly above those of B-free TiN_{0.87} having $H = 29.2 \pm 2.1$ GPa and $K_{IC} = 2.7 \pm <0.1$ MPa·m^{1/2}.

1. Introduction

Hard coatings have revolutionized materials science and engineering by enhancing the performance and durability of various materials. In particular, TiN thin films—offering an outstanding combination of mechanical properties—have found extensive usage as protective coatings for cutting tools exposed to severe mechanical and corrosive loads [1,2]. While boron (B) addition can significantly improve the hardness, wear resistance, and thermal stability of TiN-based coatings [3–7], achieving its full incorporation in the face-centered cubic (fcc) lattice is challenging [8–10]. To address this limitation, we investigate how variations either along the TiN–TiB₂ or TiN–TiB tie-line influence the solubility of B in TiN_y. We used non-reactive magnetron co-sputtering of a TiN, TiB₂, and Ti target for this task.

The larger covalent bonding radii of B (0.84 Å) compared to N (0.71 Å) cause lattice distortions in TiN when N atoms are substituted by B

[11], bringing a dielastic contribution to the solid solution strengthening mechanisms (see Fleischer's formula [12]). However, the atomic size difference and altered bond characteristics limit the full incorporation of B in the TiN lattice [13]. Typically, excess B segregates at grain boundaries [14], hindering coalescence during nucleation and coarsening during film growth. The change to a smaller-grained microstructure increases hardness by grain refinement strengthening [15,16]. Nanocomposite Ti–B–N coatings exhibit a similar effect, where TiN and TiB₂ grow simultaneously in a sequence of segregation-driven renucleation processes [17,18]. However, in reactively deposited coatings, limited B solubility in TiN induces the formation of soft amorphous BN phases [19]. Generally, the chemistry of reactively deposited coatings follows the TiN–BN tie line more. In contrast, non-reactive approaches allow compositions along the TiN–TiB₂ and TiN–TiB tie lines, achieving hard and super hard (> 40 GPa) coatings [19].

Previous studies on Ti–B–N coatings developed a well-understood

<https://doi.org/10.1016/j.actamat.2024.119858>

Received 21 September 2023; Received in revised form 1 March 2024; Accepted 20 March 2024

Available online 22 March 2024

1359-6454/© 2024 The Author(s). Published by Elsevier Ltd on behalf of Acta Materialia Inc. This is an open access article under the CC BY license (<http://creativecommons.org/licenses/by/4.0/>).

ternary phase system [3,4,17–20], providing a solid basis for understanding the impact of B on the microstructure and mechanical properties of TiN [20–23]. However, soluting higher amounts of B in the fcc lattice—without forming secondary phases—remains challenging. To overcome this challenge, we propose a non-reactive co-sputtering approach to achieve a single-phased Ti–B–N solid solution with a high amount of B incorporated in the TiN lattice.

Specifically, we aimed for Ti–B–N coatings with chemistry along two quasibinary tie lines: (i) TiN–TiB₂, via co-sputtering TiN and TiB₂ targets, and (ii) TiN–TiB, via co-sputtering TiN, TiB₂, and Ti. For easier reading, these coating systems are referred to as TiN–TiB₂ and Ti(N,B). Notably, TiN–TiB₂ refers to the analogous tie-line, not the coating composition. Varying the current applied to the TiB₂ and Ti targets—while keeping that at TiN constant—we show that additional co-sputtering of Ti increases the solubility of B in TiN up to 8.9 at.%. Ab initio density functional theory calculations underpin these observations. Furthermore, Ti over-stoichiometry (or more vacancies at the non-metal sublattice [24]) is required to maintain the high hardness of single-phased Ti–B–N and fracture toughness if the B-content exceeds ~3at.%.

2. Materials and methods

Six different Ti–B–N coatings, in addition to one TiN_y, were prepared with an AJA International Orion 5 PVD machine equipped with one 3" and two 2" unbalanced magnetron sputtering sources holding a TiN (99.5 % purity), TiB₂ (99.5 % purity), and Ti (grade 2) target (all from Plansee Composite Materials GmbH), respectively. Before loading and mounting the substrates Si (100) 7 × 20 × 0.38 mm³, mirror polished austenitic steel 7 × 20 × 0.75 mm³, and single crystalline sapphire (1̄102) 10 × 10 × 0.53 mm³ to the deposition chamber, they were ultrasonically cleaned in acetone and ethanol for 5 min each. Inside the chamber—after reaching the base pressure of below 1·10⁻⁴ Pa (1·10⁻⁶ mbar)—the substrates were thermally cleaned at ~450°C for 20 min, afterwards Ar-ion etched using an Ar pressure (20 sccm Ar-flow) of 6 Pa and applying a negative voltage of 750 V to the rotating (1 Hz) substrate-holder (keeping the substrate temperature at ~450°C). During depositions—using a current-controlled mode for sputtering the target—the substrates were negatively biased with -60 V DC. The 4-inch substrate holder is ~10 cm above the confocal target arrangement. Different chemistries of the Ti–B–N coatings are obtained by adjusting solely the sputtering-currents applied to the 2" TiB₂ (*I*_{TiB₂}) and Ti (*I*_{Ti}) targets between 0 and 0.6 A, while the TiN target was always operated with *I*_{TiN} = 0.75 A. The other deposition parameters were kept constant using a substrate bias of -60 V DC, substrate temperature of ~450°C, substrate-holder rotation of 1 Hz, and an Ar pressure of 0.4 Pa (10 sccm Ar-flow). In addition to the TiN_y coating (i.e., *I*_{Ti} = *I*_{TiB₂} = 0 A), three Ti–B–N coatings are prepared only with the TiN and TiB₂ target (i.e., *I*_{Ti} = 0 A, and *I*_{TiB₂} = 0.2, 0.4, 0.6 A), and three are prepared by synchronizing the TiB₂ and Ti target (i.e., *I*_{Ti} = *I*_{TiB₂} = 0.2, 0.4, 0.6 A). For easier distinction, the first three are referred to as TiN–TiB₂ and the last three as Ti(B, N) throughout the manuscript; overall, they will be named Ti–B–N. The deposition time was adjusted between 80 and 92 min (based on pre-studies) to prepare coatings with a thickness *t* of ~2 μm.

Their chemical composition was obtained from samples deposited on sapphire through Time-of-Flight Elastic Recoil Detection Analysis (ToF-ERDA) at the 5 MV Pelletron Tandem accelerator at Uppsala University [25] using ¹²⁷I⁸⁺ projectiles with a primary energy of 36 MeV. The beam incident angle was 67.5° to the surface normal, where recoils reached the detector at an angle of 45° with respect to the incident beam direction. The raw experimental data were analyzed using the CONTES software package [26]. Total systematic and statistical uncertainties were estimated to be below 5% of the deduced value for the major constituents. Additional chemical information was obtained from X-ray fluorescence (XRF) measurements using a PANalytical

AxiomAX-Advanced spectrometer with a rhodium (Rh) X-ray tube operating at 50 kV and 55 mA under vacuum conditions—calibrated with the three ERDA-analyzed TiN_{0.87}, TiN+TiB₂ (10.4 at.% B), and Ti (N,B) (8.9 at.% B) thin films.

Structural information of the coatings was derived from X-ray diffraction patterns collected with a PANalytical XPert Pro MPD (θ-θ diffractometer) in Bragg Brentano geometry, which was equipped with a CuKα radiation source operated with 45 kV and 40 mA. Fracture cross sections were investigated with an FEI Quanta 250 scanning electron microscopy (SEM) equipped with a field emission gun (operating at 10 kV) using fracture cross-sections of samples grown on Si (100) and with an FEI F20 transmission electron microscopy (TEM) equipped with a field emission gun (operating at 200 kV). The cross-section TEM samples were prepared by mechanical polishing down to 10 μm lamella thickness, following conventional preparation steps, and subsequent Ar ion milling (using a GATAN PIPS II). Top-view TEM lamella preparation was accomplished by focused ion beam (FIB) cutting on a Thermo Fischer Scios 2 DualBeam system, following a typical FIB TEM sample preparation recipe [27]. Initially, a 2 μm thick plane-view lamella was cut free, followed by ion milling steps to achieve a final thickness of about 75 nm. A final cleaning step at 2 kV and 27 pA and subsequent Ar ion milling at 0.5 kV using a Gatan PIPS II system resulted in <25 nm thickness in specific areas. A 200 kV field emission TEM (JEOL 2100F) equipped with an image-side C_s-corrector and Gatan Tridion system was used in the high-resolution TEM (HRTEM) study, which demonstrates a resolution of 1.2 Å at 200 kV. The aberration coefficient is set close to zero, under which the HRTEM images were taken under slightly over-focus conditions (close to the Scherzer defocus). The point spectra and electron energy-loss spectrum (EELS) mapping were recorded under scanning TEM (STEM) mode with a camera length of 2 cm and a dispersion of 0.2 eV per channel. The spectra were processed in a Digital Micrograph (DM version 3.42). The background was subtracted using the power-law model. The specimen thickness was estimated to be less than 0.5 (thickness (*t*)/mean free path(*λ*)) using zero-loss peak. All the spectra were calibrated using zero-loss spectra. EELS core-loss spectra were smoothed using low-pass filtering (per 2 channels) in DM.

Indentation modulus and hardness were obtained through computer-controlled nanoindentation using a UMIS II System equipped with a diamond Berkovich tip (calibrated using a fused silica standard sample). To minimize the substrate influence, we excluded data points with indentation depths larger than 10% of the coating thickness. To obtain the film-only Young's modulus, the raw modulus data were fitted and extended towards zero indentation depth, following the instructions given in [28,29]. Biaxial residual stresses of the coatings on sapphire substrates were obtained by measuring their curvature using a Nanovea PS50 profilometer and applying the Stoney equation [30].

The fracture toughness in terms of the critical intensity factor (*K*_{IC}) was derived from in-situ microcantilever bending tests with a Hysitron PI-85 SEM PicoIndenter inside the above-mentioned FEI Quanta 250 FEGSEM. For this, fracture cross-sections of samples grown on Si (100) were mechanically polished with a 1 μm diamond lapping film, after which, at a larger region, the Si substrate was chemically removed through etching with a 40 wt.% aqueous KOH at a temperature of 70°C. The resulting freestanding Ti–B–N thin film region was machined with a focused Ga ion beam (FEI Quanta 200 3D DBFIB) to obtain microcantilevers with dimensions of 7•*w* × *w* × *w* (i.e., the length-to-width ratio *l/w* = 7 and the breadth *b* = *w*) including a pre-notch with the depth *a* across the breadth by leaving material-bridges on each side of the notch. The cantilever shape was coarse-machined with 3 nA, and the final step was made with 0.5 nA to minimize the impact of FIB damages on the investigation; the pre-notch was milled with 50 pA to reduce geometrical errors and to ensure a small notch-radius. These cantilevers were loaded with a spherical diamond indenter with a tip radius of ~1 μm in displacement-controlled mode (5 nm s⁻¹) until fracture. The maximum load *P*_{max} and the cantilever dimensions were used to calculate *K*_{IC} after Matoy et al. [31]:

$$K_{IC} = \frac{P_{max} \cdot l}{b \cdot w^{\frac{3}{2}}} \cdot f\left(\frac{a}{w}\right)$$

with:

$$f\left(\frac{a}{w}\right) = 1.46 + 24.36 \cdot \left(\frac{a}{w}\right) - 47.21 \cdot \left(\frac{a}{w}\right)^2 + 75.18 \cdot \left(\frac{a}{w}\right)^3$$

A total of 8 cantilever tests per Ti–B–N specimen was conducted, with a success rate of 72 % and w values (after machining) of $\sim 2 \mu\text{m}$.

Density function theory (DFT) calculations were conducted employing the Vienna ab initio simulation package (VASP) [32,33] together with projector augmented plane-wave (PAW) pseudopotentials [34] and the Perdew–Burke–Ernzerhof generalized gradient approximation (GGA) [35]. A plane-wave cutoff energy of 600 eV was used together with an automatically generated Γ -centered k -point mesh (length parameter of 60 Å). The equilibrated structure of fcc-TiN (Fm-3m, $a = 4.255 \text{ \AA}$) served as a building block of a 64-atom ($2 \times 2 \times 2$) model for fcc-TiN_{1-x}B_x, fcc-TiN_{1-2x}B_x, and fcc-Ti_{1-x}NB_x solid solutions, corresponding to compositions along the TiN–TiB, TiN–TiB_{0.5}, and TiN–BN tie lines, respectively. The B atoms were distributed at the N and Ti sublattice according to the special quasirandom structure (SQS) approach [36]. All structures were fully optimized until forces on atoms were below 10^{-4} eV/\AA and the total energies of two successive ionic steps did not differ by more than $10^{-5} \text{ eV/supercell}$.

Polycrystalline Young's moduli, E , of selected solid solutions (with compositions close to the experimental findings) were evaluated from elastic constants obtained by the stress-strain method [37,38]. Assuming a brittle cleavage of the first-neighbor Ti–N/B bonds, cleavage energies, $E_{cl(001)}$, were estimated using the rigid block displacement method [39]. With the directional Young's modulus, $E_{[001]}$, and cleavage energy, $E_{cl(001)}$, we calculated the theoretical K_{IC} according to Griffith's formula [40]:

$$K_{IC(001)} = 2 \sqrt{E_{cl(001)} \cdot E_{[001]}}$$

As our supercell size allowed deriving eight $E_{cl(001)}$ values for a given B content x in TiN_{1-x}B_x (due to eight (001) planes in each supercell differing only by local distribution of B), we used these to calculate error bars of DFT $K_{IC(001)}$.

3. Results and discussion

To assess the impact of chemistries either along the TiN–TiB₂ or TiN–TiB tie line on the solubility of B within the TiN-based lattice—and consequently on the evolving microstructure and mechanical properties—we developed two non-reactively prepared Ti–B–N series, one co-sputtered from TiN and TiB₂ targets (referred to as TiN–TiB₂) and one co-sputtered from TiN, TiB₂, and Ti targets (with synchronized sputtering current at the TiB₂ and Ti target, referred to as Ti(B,N) samples), detailed described in the experimental part of the manuscript.

Fig. 1 shows that the TiN–TiB₂ samples are chemically close to the TiN–TiB₂ tie line, while the Ti(N,B) samples are close to the TiN–TiB tie line. Consequently, the Ti content of the latter is nearly constant with 52.9, 53.0, 53.6, and 52.7 at.%, for B contents of 0.0, 2.4, 5.7, and 8.9 at.%, respectively. The solely TiN+TiB₂ co-sputtered ones have decreasing Ti contents of 52.9, 52.7, 51.7, and 49.6 at.%, and increasing B-contents of 0.0, 3.0, 6.9, and 10.4 at.% with increasing I_{TiB_2} from 0.0 to 0.6 A. The N-deficiency of the non-reactively sputtered film from the TiN target (i. e., the TiN_{0.87}-sample) mainly stems from different gas-scattering and sputter-angle distributions of N and Ti [41–43]. Therefore, the chemical compositions of our coatings are closer to the TiN_{0.87}–TiB₂ respectively TiN_{0.87}–TiB tie-line (bordering the hatched region in Fig. 1) than to the TiN–TiB₂ respectively TiN–TiB tie-lines (bordering the gray-shaded region in Fig. 1). Fig. 1 further shows that the coatings obtained by co-sputtering TiN+TiB₂+Ti deviate further from the corresponding TiN_{0.87}–TiB tie line (towards the Ti-corner) with increasing B content than the coatings obtained by co-sputtering TiN+TiB₂ do deviate from

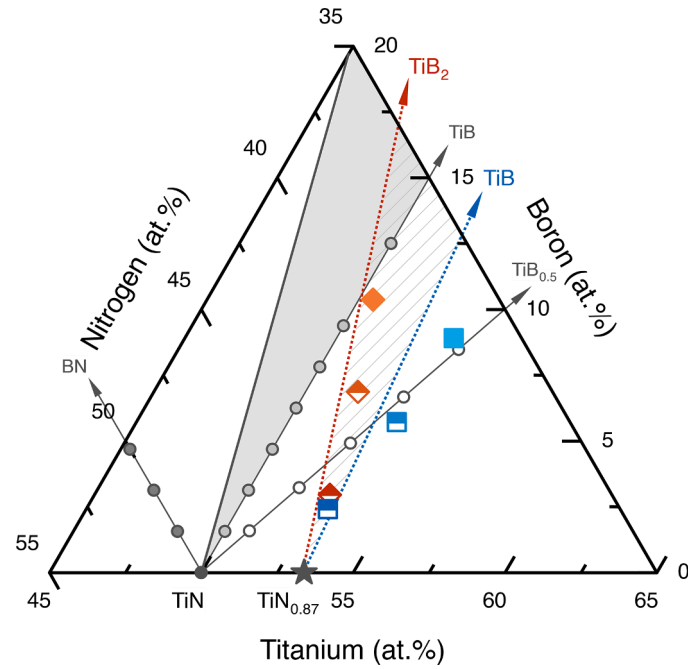


Fig. 1. Part of the isothermal Ti–B–N phase diagram, including the chemical compositions of the deposited samples as determined by ToF-ERDA (coatings marked as full-filled symbols) and XRF (the four indicated with half-filled symbols). The orange diamond symbols (close to the TiN–TiB₂ tie line) represent the TiN–TiB₂ coatings obtained by co-sputtering TiN and TiB₂, while the blue cube symbols (close to the TiN_{0.87}–TiB tie line) represent the Ti(N,B) coatings obtained by co-sputtering TiN, TiB₂, and Ti. From the non-reactively sputtered TiN_{0.87} specimen (N/Ti ratio, y , of 0.87, determined with ERDA)—represented by the gray star symbol—to the highest B-containing sample of each series (TiN–TiB₂ and Ti(B,N)), the color becomes lighter. Gray round symbols represent an excerpt from the DFT calculations contrasting the experimental values. White-filled round symbols track TiN_{1-2x}B_x values along the TiN–TiB_{0.5} line, indicating that for each B substituting N, an N-vacancy is “added”. Gray-filled symbols correspond to TiN_{1-x}B_x values along the TiN–TiB tie line, where B substitutes N. Dark gray-filled symbols follow Ti_{1-x}NB_x along the TiN–BN tie line, indicating that B-substitutes Ti.

their corresponding TiN_{0.87}–TiB₂ tie line. The gray round data points in Fig. 1 represent the course of our DFT calculations, highlighting the coherence of our deposited coatings and theoretically calculated data points (discussed below).

XRD analyses of the TiN–TiB₂ and Ti(N,B) coatings indicate that both series maintain the single-phase cubic fcc-TiN structure without the formation of other crystalline phases with increasing B content, see Fig. 2. While the TiN–TiB₂ coatings show no distinct oriented growth, the Ti(N,B) coatings indicate a 200-oriented growth for both highest B contents (5.7 and 8.9 at.%).

More detailed peak profile analysis with respect to lattice plane distance d_{200} (Fig. 3a) and full width at half maximum Γ_{200} (Fig. 3b) highlights significant differences between the two coating series. For TiN–TiB₂, d_{200} initially increases from 2.129 to 2.142 Å upon adding 3.0 at% B, after which it slightly decreased again to 2.136 Å (at 10.4 at% B), while Γ_{200} continuously increased. Contrary, the Ti(N,B) samples experience a continuously increasing d_{200} (up to 2.158 Å at 8.9 at% B) while their Γ_{200} stayed at $0.55^\circ \pm 0.08^\circ$ upon increasing the B content to 8.9 at%, compare Figs. 3a and b. Increasing lattice plane distances of the Ti–N–B coatings with increasing B content indicate that B is incorporated in the TiN lattice, due to the larger covalent bonding radii of B as compared to N [14], rather than being segregated to the grain boundaries. As discussed later, the change towards smaller 2θ is not attributed to increased residual stresses.

Consistent with the observed trendline for our Ti(N,B) coatings

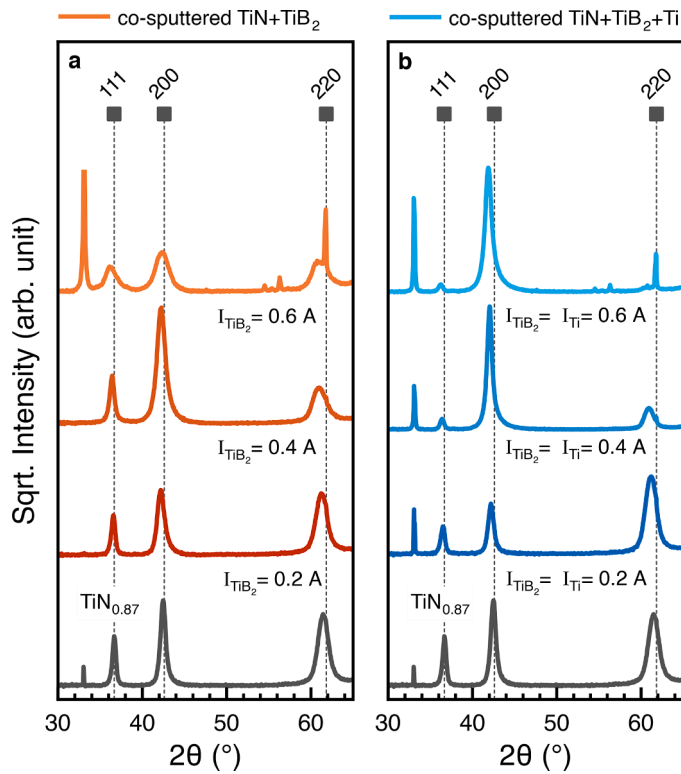


Fig. 2. X-ray diffraction (XRD) patterns of Ti-B-N coatings co-sputtered from TiN+TiB₂ and those co-sputtered from TiN+TiB₂+Ti, given in orange and blue, respectively. XRD patterns of the (a) TiN-TiB₂ and (b) Ti(N,B) coatings with labeled currents applied to the TiB₂ target, I_{TiB_2} . For TiN-TiB₂ $I_{\text{Ti}} = 0$ A and for Ti(N,B) I_{Ti} was synchronized with I_{TiB_2} , I_{TiN} was always 0.75 A. Standard positions of TiN (111), (200), and (220) crystal planes (JCPDS no. 00-038-1420) are indicated.

(Fig. 3a), ab initio calculations in Fig. 4a show that the d_{200} lattice spacing almost linearly increases with increasing B content in the case of fcc-TiN_{1-x}B_x and fcc-TiN_{1-2x}B_x structures, where the latter exhibits N vacancies (having a very minor effect on d_{200}). Contrarily, the opposite trend—qualitatively inconsistent with our experimental observations for Ti(N,B)—is predicted for fcc-Ti_{1-x}NB_x. Mind that we do not expect a perfect quantitative agreement between DFT and experimental d_{200} due to many effects omitted by our DFT models, such as finite temperatures, residual stresses, and the coating's inherent microstructure. In combination with the comparison between ab initio and experimental d_{200} variation, the preferential B-for-N substitution—if B is incorporated in the fcc-TiN lattice—is provided by assessing relative chemical stability, as estimated by (zero Kelvin) formation energy, E_f , see Fig. 4b. The least negative E_f of fcc-Ti_{1-x}NB_x (compared to fcc-TiN_{1-x}B_x and fcc-TiN_{1-2x}B_x) again points towards that B substitutes for Ti is the least likely scenario. The N-vacancy-containing fcc-TiN_{1-2x}B_x yields E_f slightly above that of fcc-TiN_{1-x}B_x. These differences may further diminish at finite temperatures when considering configuration entropy contribution, thus, fcc-TiN_{1-2x}B_x becoming energetically closer (or even favored) over fcc-TiN_{1-x}B_x. However, we focus exclusively on fcc-TiN_{1-x}B_x for comparison with our subsequent experimental results.

The slightly decreasing d_{200} values of TiN-TiB₂ samples upon increasing their B-content beyond 3.0 at.% in combination with the continuously increased Γ_{200} values, compare Figs. 3a and b, suggest that only approx. 3 at.% B is substituting for N in the TiN_y lattice, while the surplus promotes the formation of an additional X-ray amorphous boundary phase. The mechanisms are similar to what has been studied in detail for TiN-SiN_y [44–46]. Such segregations during film growth interfere with coalescence and promote re-nucleation, leading to smaller crystallite sizes. These would result in larger Γ_{200} values, as observed for

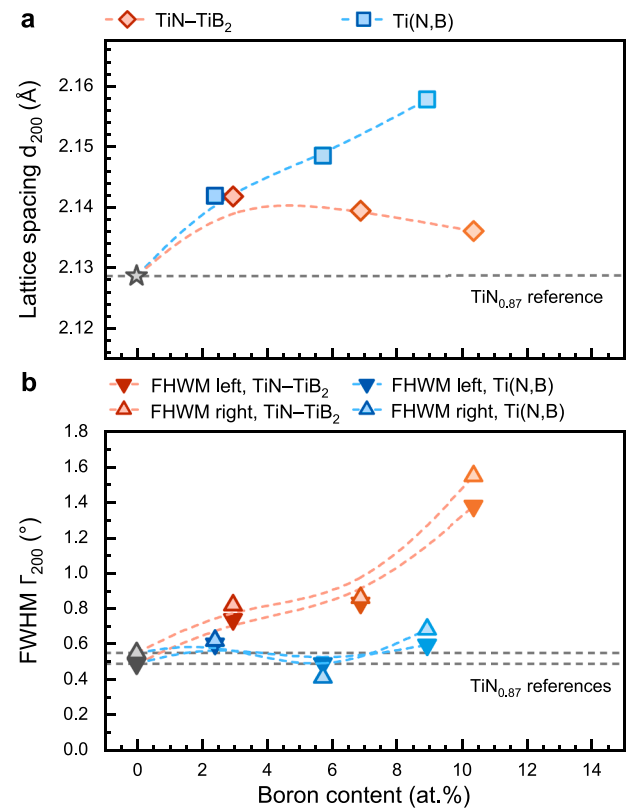


Fig. 3. (a) Lattice plane distances d_{200} and (b) full width at half maximum (FWHM) of the 200-peak. The orange diamond (a) and triangular (b) symbols represent the TiN-TiB₂ coatings, while the blue cube (a) and triangular symbols represent the Ti(N,B) coatings. The values were determined through peak profile fitting using a Pearson 7 function and an asymmetry type of peaks by split width and shape. The gray star symbol represents the data point for sputtered TiN_{0.87}.

TiN-TiB₂. Contrary, the small and nearly constant Γ_{200} , in combination with increasing d_{200} as the B content increases for Ti(N,B), indicates that B is fully incorporated in the crystal lattice (as mentioned above, substituting for N).

To underpin the difference in B solubility for the TiN-TiB₂ respectively Ti(N,B) samples, those with the highest B content were studied in detail by TEM. The 10.4 at.% B-containing TiN-TiB₂ coating's cross-section (Fig. 5a) exhibits a compact, dense growth morphology with small grains, on average 18 ± 7 nm; see the dark-field cross-sectional TEM Fig. 5b. This additionally shows a more featherlike microstructure. Contrary, the 8.9 at.% B-containing Ti(N,B) coating's cross-section (Fig. 5c) exhibits a more columnar growth morphology with column diameters of 54 ± 15 nm on average (see the dark-field image, Fig. 5d). Complementary top-view images display the overall morphology of the grains, revealing a refined microstructure with distinct and thick grain boundaries of the TiN-TiB₂ sample (Fig. 5e and 5f), as a result of segregation effects inhibiting also the columnar growth during film deposition. In contrast, the plane view microstructure of the Ti(N,B) sample showcases larger grains arranged with significantly less-distinct and also much thinner grain boundaries, as shown in Fig. 5g and 5h. The microstructural differences between the two Ti-B-N coatings suggest that the additional Ti increases the solubility of B within the TiN-lattice during film growth, resulting in reduced segregation processes and thus larger-grained microstructure with prominent columnar growth.

The selected area electron diffraction (SAED) pattern in Fig. 6a—obtained with a 750 nm diameter aperture positioned in the center of the cross-section, including the integrated intensity of the full ring pattern—demonstrates a TiN structure without signs of another

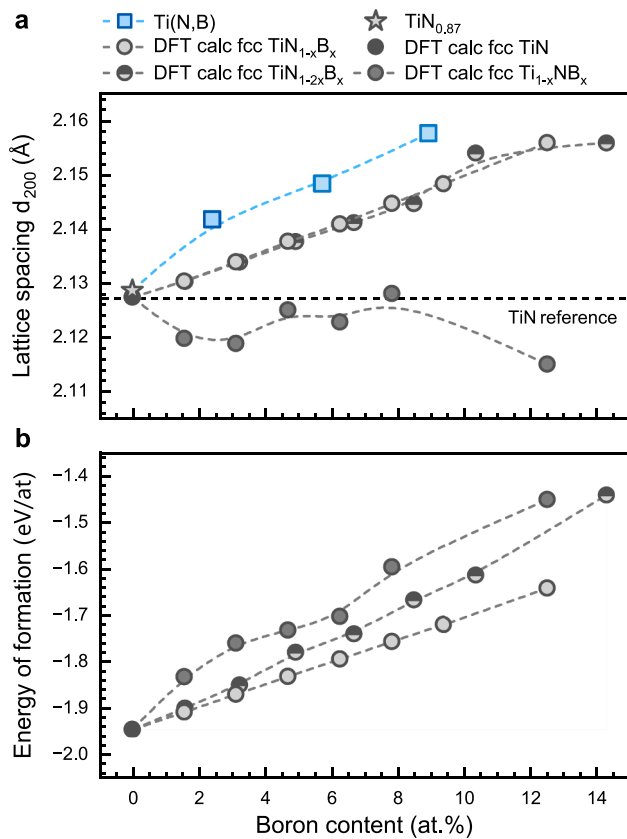


Fig. 4. DFT-calculated (a) d_{200} lattice spacing, and (b) energy of formation (E_p) as a function of B content for three Ti-B-N structural variants: (i, round gray-filled symbols) $\text{TiN}_{1-x}\text{B}_x$, where B replaces N at the non-metal sublattice, (ii, round dark gray-filled symbols) $\text{Ti}_{1-x}\text{NB}_x$, where B replaces Ti at the metal sublattice, (iii, half-filled gray circular symbols) $\text{TiN}_{2-x}\text{B}_x$, where B occupies the non-metal sublattice with the formation of N-vacancies. The blue trend line (starting from $\text{TiN}_{0.87}$, symbolized by a gray star) reflects the Ti(N,B) coatings from Fig. 3a.

crystalline phase. The nearly closed diffraction rings, which are relatively broad, mark a small grain size. Similar to the TiN-TiB_2 coating sample, SAED investigations of Ti(N,B) (Fig. 6b, with an overlay of the integrated intensity) show no other crystalline phases than fcc-TiN, in agreement with XRD measurements. Contrary to the TiN-TiB_2 coating, the diffraction rings for Ti(N,B) are sharper with even distinct diffraction spots, indicating (again in agreement with XRD) higher crystalline quality and larger grains/columns. Similar results can be seen in the top-view SAED patterns (obtained with a 200 nm diameter aperture) of both Ti-B-N thin films (compare Fig. 6c and 6d). The combination of the SAEDs also indicates smaller diffraction ring radii for Ti(N,B) than for TiN-TiB_2 , which is equivalent to larger lattice parameters, especially seen when comparing the larger diffraction rings and the peak positions of the integrated intensity. These SAED investigations for TiN-TiB_2 and Ti(N,B) are in excellent agreement with XRD. Because the SAED is obtained from the cross-section, no preferred growth orientation is visible for the 8.9 at.% B-containing Ti(N,B) , contrary to the XRD studies. However, the preferred [200] and [220] orientations can be seen in the SAED obtained from the top-view sample (Fig. 6d).

To further substantiate the difference in B solubility of the two differently co-sputtered Ti-B-N series, we compare the grain boundary structures and the B distribution of the TiN-TiB_2 and Ti(N,B) coatings with 10.4 and 8.9f at.% B, respectively, by high-resolution top-view

TEM investigation. Fig. 7a shows the atomic-scale HRTEM image HRTEM image displaying a triple junction with amorphous phases. By EELS mapping the selected area outlined in Fig. 7b, the elemental distribution of B is visualized in Fig. 7c, significantly highlighting the B enrichment at the triple junction. In addition, individual core-loss spectra (Fig. 7d) illustrate an enhanced intensity of the B-K edge at the triple junction compared to the nearby grain.

In contrast, the HRTEM image of the Ti(B,N) coating, shown in Fig. 8a, shows an overall crystalline microstructure with no amorphous grain boundary phases. Furthermore, the corresponding EELS mapping and individual spectra (Figs. 8b-8d) do not show any significant B enrichment at the triple junctions of the columnar grains. This observation indicates that B is distributed homogeneously—akin to being fully soluted—in the fcc- Ti(N,B) coating, compared to the pronounced B segregation in the TiN-TiB_2 coating. We further suggest that the B segregation promotes the amorphization of the grain boundary structure.

How these differences in microstructure and soluted B content between TiN-TiB_2 and Ti(N,B) are reflected in the mechanical properties and fracture toughness was studied with nanoindentation and in-situ micromechanical bending tests.

Despite the difference in grain size, preferred growth orientation, and soluted B, both coating series show a similar increase in H with increasing B content, Fig. 9a. The hardness of TiN-TiB_2 with the highest B content (10.4 at.%) is 36.9 ± 1.9 GPa while that of Ti(N,B) with the highest B content (8.9 at.%) is 37.1 ± 1.9 GPa. The unchanged Γ_{200} (Fig. 3b) and nearly unchanged compressive residual stresses (Fig. 9b) indicate comparable grain sizes and micro stresses for Ti(N,B) regardless of their B content. Hence, the steady shift in peak position, see Fig. 3a, is linked to the increasing amount of B incorporated within the lattice rather than caused by residual stresses. On the contrary, the TiN-TiB_2 coatings exhibit an initial decline in compressive residual stresses from -2.92 GPa (for $\text{TiN}_{0.87}$) to -1.74 GPa upon adding 3.0 at.% B, after which σ slightly increased to -2.53 (for 10.4 at.% B).

Contrary to the residual compressive stresses, the Young's modulus (E) only slightly varies for the individual TiN-TiB_2 coatings but markedly decreases for Ti(N,B) from 478 GPa ($\text{TiN}_{0.87}$) to 438 GPa upon increasing the B content to 8.9 at.%, Fig. 9c. This decline in E with increasing B content is also captured by ab initio calculations for fcc- $\text{TiN}_{1-x}\text{B}_x$.

Together, these data indicate that the TiN-TiB_2 coatings experience solid solution strengthening (up to 3 at.% B) and grain refinement strengthening. For the Ti(N,B) coatings, solid solution strengthening is dominating up to their maximum B content of 8.9 at.%, because their grain size is essentially unchanged and B is fully soluted, as mentioned above during the discussion of their XRD and TEM results. Ab initio investigations furthermore suggest N with B substitution for these Ti(N,B) samples through their excellent agreement with fcc- $\text{TiN}_{1-x}\text{B}_x$ structures. As suggested by the classical Fleischer equation, the deviation of the hardness increase from a $B^{0.5}$ dependence suggests other contributions, which could be an additional increase in dislocation density and increased vacancy content.

The two coating series, TiN-TiB_2 and Ti(N,B) , provide an opposing trend for their fracture toughness K_{IC} with increasing B content. The $\text{TiN}_{0.87}$ coating exhibits a K_{IC} of $2.7 \pm 0.1 \text{ MPa}\cdot\text{m}^{1/2}$, which decreases to $2.1 \pm 0.1 \text{ MPa}\cdot\text{m}^{1/2}$ upon increasing B to 10.4 at.% for the TiN-TiB_2 samples but increases to $3.0 \pm 0.2 \text{ MPa}\cdot\text{m}^{1/2}$ upon increasing B to 8.9 at.% for the Ti(N,B) samples, Fig. 10a. The ab initio derived cleavage energy for fcc- $\text{TiN}_{1-x}\text{B}_x$ also provides such a trend of increasing values with increasing B content, Fig. 10b. Again, in addition to d_{200} and Young's modulus, there is a nice agreement between Ti(N,B) samples (with chemistries along the $\text{TiN}_{0.87}\text{-TiB}$ tie line) and the fcc- $\text{TiN}_{1-x}\text{B}_x$ solid

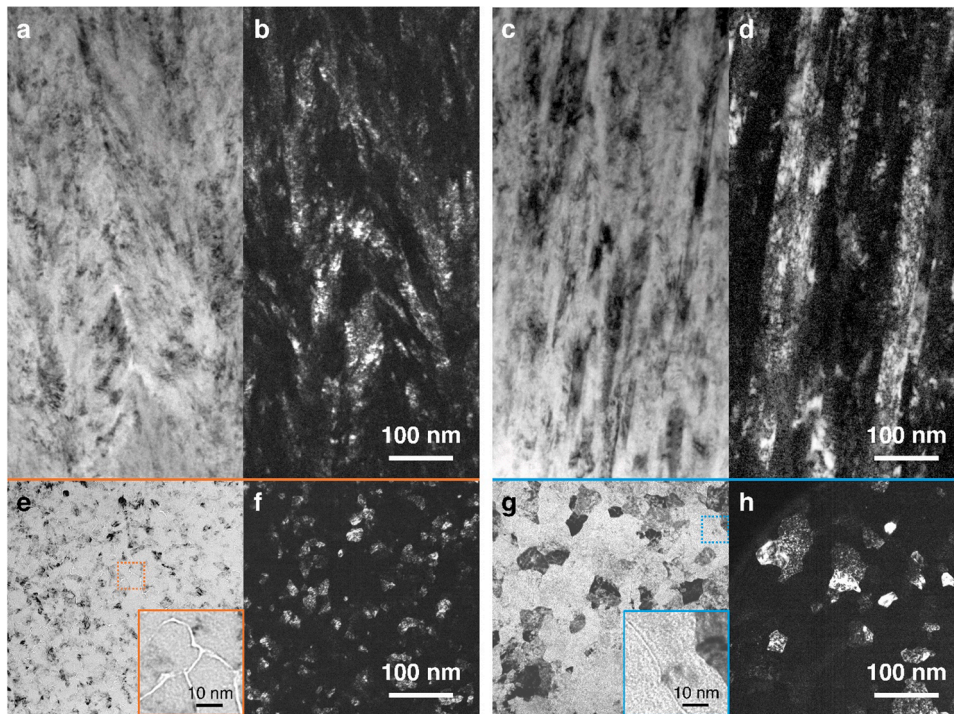


Fig. 5. TEM investigations of the TiN-TiB₂ coating with 10.4 at.% B. (a) Bright-field TEM image from the middle region of the coating's cross-section. (b) Dark-field TEM variant with 111 and 200 reflections of the same area as in (a). Same for Ti(N,B) coating with 8.9 at.% B. (c) Bright-field and corresponding (d) dark-field TEM image. (e) Top-view TEM bright-field micrograph from a near-surface region of the same TiN-TiB₂ sample and (f) dark-field TEM image highlighting the 111 and 200 reflections of the same area as in (e). The inset in (e) framed in solid-orange is a higher magnification of the section indicated with dashed-orange and illustrates the distinct and thick grain boundaries. Analogous top-view bright-field (g) (with corresponding blue framed inset) and dark-field (h) TEM images for the Ti(N,B) sample with 8.9 at.% B are provided.

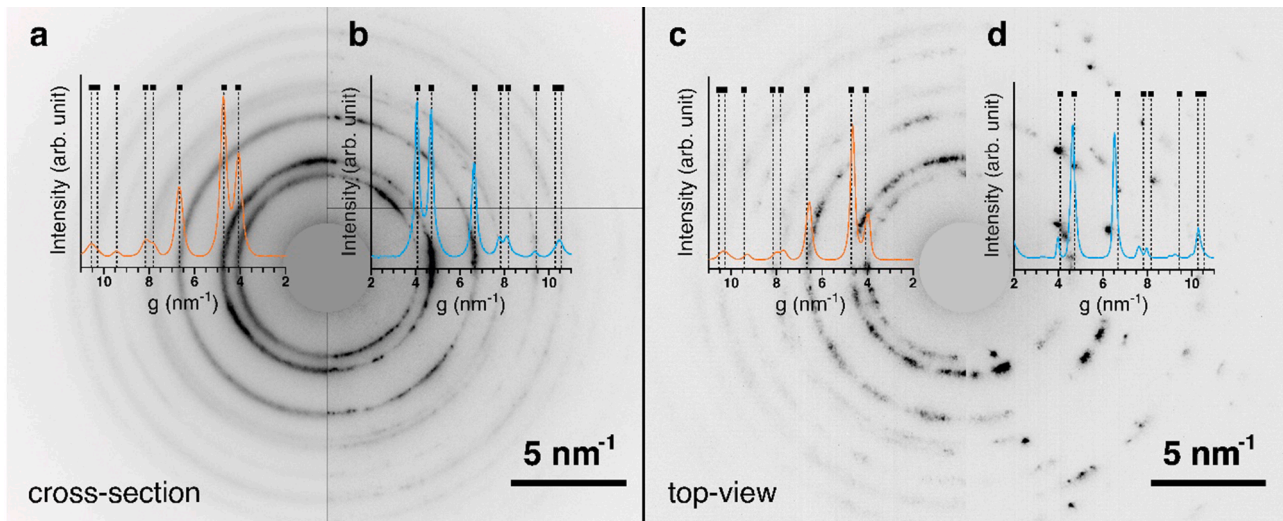


Fig. 6. Comparative selected-area electron diffraction (SAED) analysis from cross-section TEM-samples of (a) TiN-TiB₂ coating with 10.4 at.% B and (b) Ti(N,B) coating with 8.9 at.% B, including an overlay of the integrated intensity in orange (a) and blue (b), respectively (CrystBox [38]). A similar SAED analysis is compared for the top-view TEM samples for TiN-TiB₂ (c) in orange and Ti(N,B) (d) in blue. The squared symbols mark the fcc-TiN reference (JCPDS no. 00-038-1420).

solution where B substitutes for N. Thus, for these Ti(N,B) samples the provided B (here studied up to 8.9 at.%) is fully soluted in the TiN_y lattice. On the contrary, the TiN-TiB₂ coatings with compositions along the TiN_{0.87}-TiB₂ tie line can only solute up to approx. 3 at.% B, as suggested by the comparison between XRD and DFT calculated d_{200} of fcc-TiN_{1-x}B_x solid solutions. A surplus in B is accommodated by an amorphous B-rich grain boundary phase, as detected by EELS (Figs. 7b-

7d). This excess amount of B at the grain boundaries obviously negatively influences their fracture toughness, because the TiN-TiB₂ sample with the highest B content (10.4 at.%) provides the lowest K_{IC} value of only $2.1 \pm 0.1 \text{ MPa}\cdot\text{m}^{1/2}$, regardless of providing one of the highest H and E values combined with smallest grain size and dense growth morphology. Classically, the combination of such characteristics (while the residual stresses are comparable) would favor an increased fracture

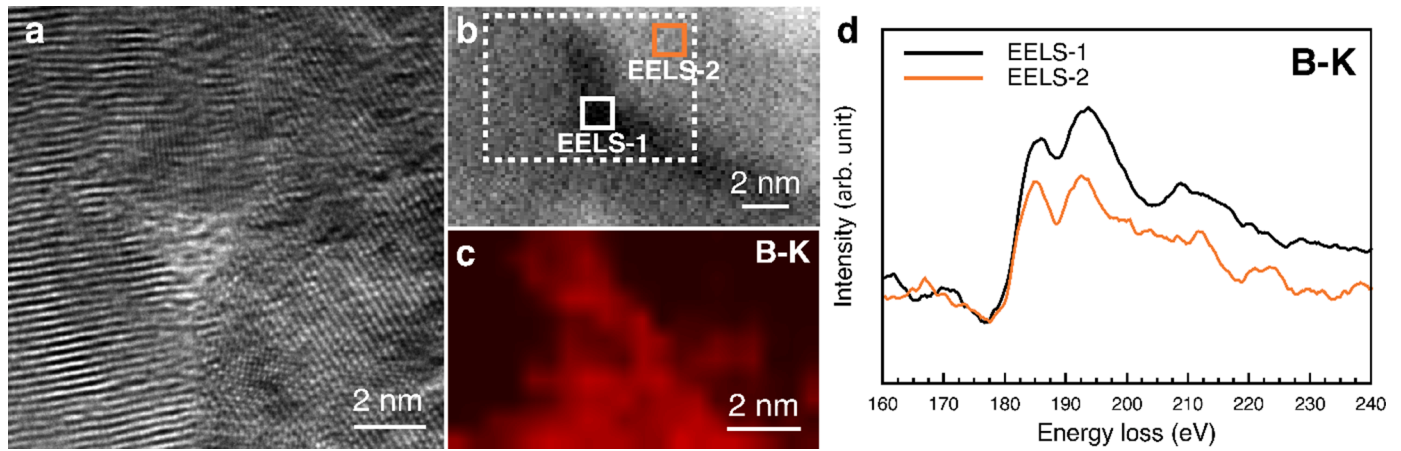


Fig. 7. (a) Top-view high-resolution TEM (HRTEM) image showing TiN–TiB₂ coating with 10.4 at.% B of a triple junction. (b) and (c) show high-angle annular dark-field (HAADF) images covering the area around a triple junction and EELS B–K edge mapping of the corresponding area indicated by a white-lined box, respectively. (d), EELS spectral (B–K edge) results of the triple junction (EELS-1) and the nearby grain (EELS-2).

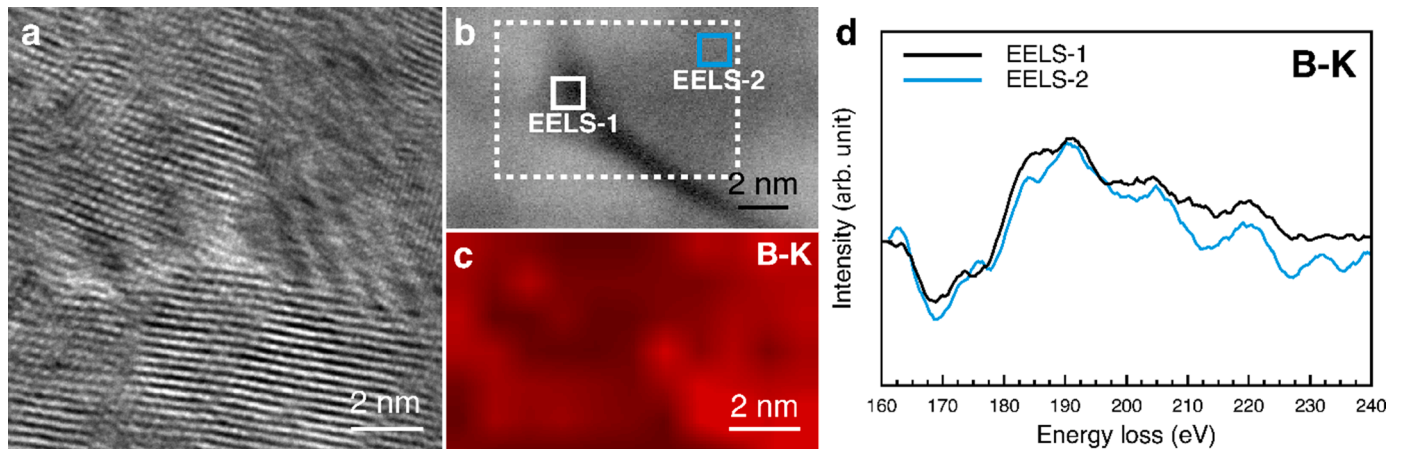


Fig. 8. (a) Top-view high-resolution TEM (HRTEM) image at the triple junction of the 8.9 at.% B fcc-Ti(N,B) columnar grains. (b) and (c), HAADF imaging and EELS B–K edge mapping of the corresponding white dashed area. (d), EELS spectral (B–K edge) results of a region within the triple junction (EELS-1) and a nearby grain (EELS-2).

toughness if no additional weaker phase is present.

4. Summary and conclusions

This study addressed the open question on B-solubility in TiN_y by developing two Ti–B–N series, one along the TiN–TiB₂ and one along the TiN–TiB tie line. Experimentally, this was achieved through non-reactive co-sputtering of TiN and TiB₂ respectively TiN, TiB₂, and Ti. Accurate assessment of the chemical composition by ERDA proved a N/Ti ratio of 0.87 for the film prepared by non-reactive sputtering the TiN target and a max. B content of 10.4 and 8.9 at.% in the TiN–TiB₂ and Ti(N,B) coatings, respectively. Together with XRF analysis, this showed that while the TiN–TiB₂ films are chemically very close to the TiN_{0.87}–TiB₂ line, the Ti(N,B) films deviate from the TiN_{0.87}–TiB tie line towards the Ti corner with increasing B content (as the sputtering current applied to the Ti target was synchronized with that applied to the TiB₂ target). The latter should turn out to be decisive for an increased B solubility within TiN_y in the end.

Detailed XRD, TEM, SAED, and HRTEM studies indicated that the only crystalline phase present is fcc-TiN_y-based and that the highest B-containing TiN–TiB₂ and Ti(N,B) film has a grain size of 18±7 nm and column diameter of 54±15 nm, respectively. This 10.4 at.% B

containing TiN–TiB₂ was randomly oriented with rather equiaxed grains while the 8.9 at.% B containing Ti(N,B) has a pronounced (200) growth orientation with columnar grains.

Comparison of their *d*₂₀₀ lattice spacings with theoretical (DFT-predicted) values for fcc-Ti_{1-x}N_xB_x, fcc-TiN_{1-x}B_x, and fcc-TiN_{1-2x}B_x pointed out that the Ti(N,B) coatings can completely dissolve the provided 8.9 at.% B in the fcc lattice, whereas this is only possible with about 3 at.% for TiN–TiB₂. Consistently, the full width at half maximum of the XRD peaks, which increased continuously with increasing B content for TiN–TiB₂, but remained constant for Ti(N,B). Finally, our HRTEM and EELS mapping results have conclusively confirmed our XRD results and DFT predictions that only with additional co-sputtering of Ti an fcc-Ti(N,B) solid solution with 8.9 at.% B is achieved—evidenced by the distinct crystalline microstructure and homogeneous B distribution observed in the EELS mapping. In contrast, for the TiN–TiB₂ coating (10.4 at.% B), we showed that most of the B accumulates at the grain boundaries, forming an amorphous B phase, rather than being fully incorporated into the fcc-TiN crystalline grains. This surplus B interferes with coalescence processes during nucleation and growth of the TiN–TiB₂ thin film, resulting in a reduced columnar structure (nearly equiaxed grains for the max. B content) and smaller grains.

The hardness evolution with the B content was similar for both

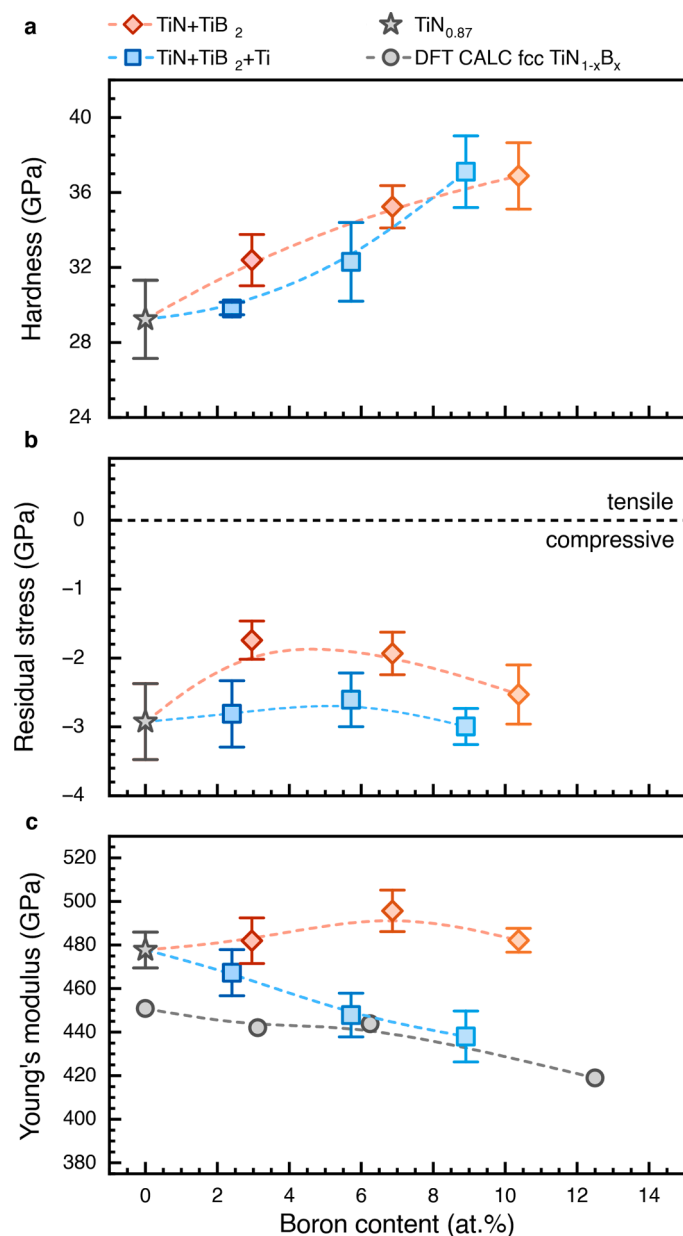


Fig. 9. Relationship between B content and hardness (a), residual stresses (b), and Young's modulus (c) of TiN-TiB₂ (orange diamond data points) and Ti(N,B) (blue cube data points) thin films. The gray star data point represents TiN_{0.87}. The ab initio calculated Young's moduli for fcc-TiN_{1-x}B_x (gray circular symbols) are added to (c).

coating series since solid-solution strengthening prevails for Ti(N,B) and grain-refinement strengthening for TiN-TiB₂. In addition to the structural similarities between Ti(N,B) and ab initio fcc-TiN_{1-x}B_x, their Young's moduli agreed with the theoretical DFT values and their decrease with increasing B content, too. The TiN-TiB₂ ones provide almost constant values across the B variation studied.

Regardless of the similar hardness values (and trend) but even larger Young's moduli combined with smaller grains, the TiN-TiB₂ coatings provide a lower fracture toughness than Ti(N,B). The difference was most pronounced for the highest B-containing coatings because K_{IC} increases with B for Ti(N,B) to $3.0 \pm 0.2 \text{ MPa}\cdot\text{m}^{1/2}$ but decreases for TiN-TiB₂ to $2.1 \pm 0.1 \text{ MPa}\cdot\text{m}^{1/2}$. For B-free fcc-TiN_{0.87}, $K_{IC} = 2.7 \pm 0.1 \text{ MPa}\cdot\text{m}^{1/2}$.

Based on our findings, successfully incorporating advantageous

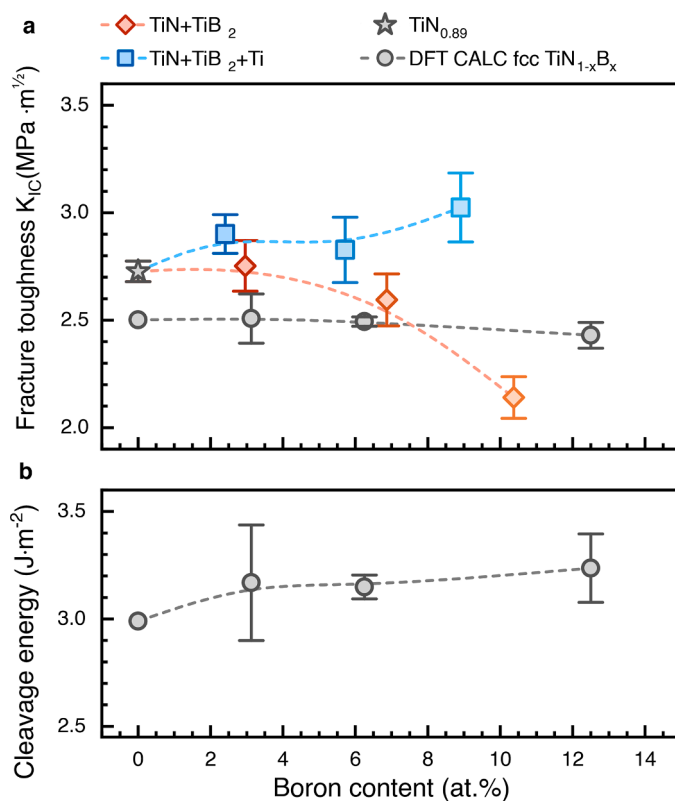


Fig. 10. (a) Fracture toughness (K_{IC}) for TiN-TiB₂ and Ti(N,B) samples. The gray star symbol represents the data point for TiN_{0.87}. (b) DFT-predicted cleavage energy, E_{cl} , of fcc-TiN_{1-x}B_x, with error bars representing standard deviation of E_{cl} values for all (100) planes in the simulation cell (due to random distribution of B atoms at the N sublattice, the planes exhibit locally slightly different chemistry). The corresponding calculated $K_{IC(100)}$ is added to (a).

elements into crystal lattices must account for their needed space. In this case, the larger B atom relative to N requires understoichiometric TiN.

CRediT authorship contribution statement

Rebecca Janknecht: Conceptualization, Investigation, Writing – original draft, Visualization. **Rainer Hahn:** Supervision, Conceptualization, Investigation, Writing – review & editing. **Nikola Koutná:** Investigation, Writing – review & editing. **Tomasz Wójcik:** Investigation. **Eleni Ntemou:** Investigation. **Andreas Steiger-Thirnsfeld:** Investigation. **Zhuo Chen:** Investigation. **Alexander Kirnbauer:** Writing – review & editing. **Peter Polcik:** Writing – review & editing, Resources. **Szilárd Kolozsvári:** Writing – review & editing, Resources. **Zaoli Zhang:** Investigation, Writing – review & editing, Resources. **Daniel Primetzhofer:** Writing – review & editing, Resources. **Paul H. Mayrhofer:** Supervision, Conceptualization, Writing – review & editing, Project administration, Funding acquisition.

Declaration of competing interest

The authors declare that they have no known competing financial interests or personal relationships that could have appeared to influence the work reported in this paper.

Acknowledgements

The authors acknowledge TU Wien Bibliothek for financial support through its Open Access Funding Program. We sincerely thank the X-ray Center (XRC) at TU Wien for beam time and the Electron Microscopy

Center at USTEM TU Wien for SEM and TEM access. The computational results presented have been achieved using the National Academic Infrastructure for Supercomputing in Sweden (NAISS) at the Linköping University partially funded by the Swedish Research Council through grant agreement no. 2022-06725 and the Vienna Scientific Cluster (VSC) in Austria. The authors thank the RADIATE project for funding our

beamtime at the Tandem Laboratory at Uppsala University. Accelerator operation at Uppsala University was supported by the Swedish research council VR-RFI (no. 2019-00191). Zhuo Chen and Zaoli Zhang acknowledge the financial support of the Austrian Science Fund (FWF P 33696).

Appendix

Table A1

Summary of experimental results from the deposited samples in this study, including TiN_{0.87}, TiN–TiB₂, and Ti(N,B), with the latter two each showing increasing B concentrations.

Sample	I _{target} (Å)			B (at.%)	N (at.%)	Ti (at.%)	d ₂₀₀ (Å)	FWHM (°2θ)		H (GPa)	σ (GPa)	E (GPa)	K _{IC} (MPa•m ^{1/2})
	TiN	TiB ₂	Ti					left	right				
TiN	0.75	0	0	0	46.6	53.4	2.129	0.49	0.55	29.23	-2.92	477.68	2.73
TiN–TiB ₂	0.75	0.2	0	3.0	44.3	52.7	2.142	0.74	0.82	32.39	-1.74	481.97	2.75
		0.4		6.9	41.4	51.7	2.139	0.83	0.86	35.24	-1.93	495.65	2.59
		0.6		10.4	39.1	50.5	2.136	1.38	1.55	36.88	-2.53	482.16	2.14
Ti(N,B)	0.75	0.2	0.2	2.4	44.6	53.0	2.142	0.60	0.62	29.81	-2.81	467.27	2.90
		0.4	0.4	5.7	40.7	53.6	2.148	0.49	0.41	32.30	-2.61	447.84	2.83
		0.6	0.6	8.9	37.2	53.9	2.158	0.60	0.68	37.11	-2.99	437.97	3.02

Table A2

Summary of ab initio calculations of fcc Ti_{1-x}NB_x, TiN_{1-x}B_x, and TiN_{1-2x}B_x solid solutions in this study. According to the data presented in the manuscript, fracture toughness, K_{IC}, and cleavage energy, E_{cl}, are not calculated for all possible structures and are noted with “nc.” All values are rounded to two decimal places for clarity.

Structure	B (at.%)	N (at.%)	Ti (at.%)	Ef (eV/at)	a (Å)	K _{IC} (MPa•m ^{1/2})	E _{cl} (J•m ⁻²)
fcc-TiN	0.00	50.00	50.00	-1.94	4.26	2.50	2.99
fcc-TiN _{1-x} B _x	1.56	48.44	50.00	-1.91	4.26	nc	
	3.13	46.88		-1.87	4.27	2.51	3.17
	4.69	45.31		-1.83	4.28	nc	
	6.25	43.75		-1.80	4.28	2.49	3.15
	7.81	42.19		-1.76	4.29	nc	
	9.38	40.63		-1.72	4.30		
	12.50	37.50		-1.64	4.31	2.42	3.24
fcc-TiN _{1-2x} B _x	1.59	47.62	50.79	-1.90	4.26	nc	
	3.23	45.16	51.61	-1.85	4.27		
	4.92	42.62	52.46	-1.79	4.28		
	6.67	40.00	53.33	-1.74	4.28		
	8.47	37.29	54.24	-1.67	4.29		
	10.34	34.48	55.17	-1.61	4.31		
	14.29	28.57	57.14	-1.44	4.31		
fcc-Ti _{1-x} NB _x	1.56	50.00	48.44	-1.83	4.24	nc	
	3.13		96.88	-1.76	4.24		
	4.69		95.31	-1.73	4.25		
	6.25		93.75	-1.70	4.25		
	7.81		92.19	-1.60	4.26		
	12.50		87.50	-1.45	4.23		

References

- [1] J.-E. Sundgren, A. Rockett, J.E. Greene, U. Helmersson, Microstructural and microchemical characterization of hard coatings, *Journal of Vacuum Science & Technology A: Vacuum, Surfaces, and Films* 4 (1986) 2770–2783.
- [2] I. Petrov, L. Hultman, U. Helmersson, J.E. Sundgren, J.E. Greene, Microstructure modification of TiN by ion bombardment during reactive sputter deposition, *Thin Solid Films* 169 (1989) 299–314.
- [3] J. Neidhardt, Z. Czigány, B. Sartory, R. Tessadri, M. O’Sullivan, C. Mitterer, Nanocomposite Ti-B-N coatings synthesized by reactive arc evaporation, *Acta Mater* 54 (2006) 4193–4200.
- [4] P.H. Mayrhofer, M. Stoiber, Thermal stability of superhard Ti-B-N coatings, *Surf Coat Technol* 201 (2007) 6148–6153.
- [5] P.H. Mayrhofer, M. Stoiber, C. Mitterer, Age hardening of PACVD TiBN thin films, *Scr Mater* 53 (2005) 241–245.
- [6] P.H. Mayrhofer, C. Mitterer, J.G. Wen, I. Petrov, J.E. Greene, Thermally induced self-hardening of nanocrystalline Ti-B-N thin films, *J Appl Phys* 100 (2006).
- [7] W. Gissler, Structure and properties of Ti-B-N coatings, 1994.
- [8] R.F. Zhang, S.H. Sheng, S. Veprek, Stability of Ti-B-N solid solutions and the formation of nc-TiN/a-BN nanocomposites studied by combined ab initio and thermodynamic calculations, *Acta Mater* 56 (2008) 4440–4449.
- [9] W. Sun, C.J. Bartel, E. Arca, S.R. Bauers, B. Matthews, B. Orvañanos, B.R. Chen, M. F. Toney, L.T. Schelhas, W. Tumas, J. Tate, A. Zakutayev, S. Lany, A.M. Holder, G. Ceder, A map of the inorganic ternary metal nitrides, *Nat Mater* 18 (2019) 732–739.
- [10] M. Aykol, S.S. Dwaraknath, W. Sun, K.A. Persson, Thermodynamic limit for synthesis of metastable inorganic materials, 2018.
- [11] B. Cordero, V. Gómez, A.E. Platero-Prats, M. Revés, J. Echeverría, E. Cremades, F. Barragán, S. Alvarez, Covalent radii revisited, *Journal of the Chemical Society. Dalton Transactions*. (2008) 2832–2838.
- [12] R.L. Fleischer, Substitutional solution hardening, *Acta Metallurgica* 11 (1963) 203–209.
- [13] W. Hume-Rothery, G.V. Raynor, *The Structure of Metals and Alloys*, 1962.
- [14] S. Yang, T. Guo, X. Yan, K. Gao, X. Pang, High-density twin boundaries in transition metal nitride coating with boron doping, *Acta Mater* 255 (2023).
- [15] E.O. Hall, *The Deformation and Ageing of Mild Steel: III Discussion of Results*, *Proceedings of the Physical Society. Section B*. 64 (1951) 747. –747.

- [16] N.J. Petch, The influence of grain boundary carbide and grain size on the cleavage strength and impact transition temperature of steel, *Acta Metallurgica* 34 (1986) 1387–1393.
- [17] H.D. Männling, D.S. Patil, K. Moto, M. Jilek, S. Veprek, Thermal stability of superhard nanocomposite coatings consisting of immiscible nitrides, *Surf Coat Technol* 146–147 (2001) 263–267.
- [18] P.H. Mayrhofer, H. Willmann, C. Mitterer, Recrystallization and grain growth of nanocomposite Ti–B–N coatings, *Thin Solid Films* 440 (2003) 174–179.
- [19] R. Hahn, A. Tymoszuk, T. Wojcik, A. Kirnbauer, T. Kozák, J. Čapek, M. Sauer, A. Foelske, O. Hunold, P. Polcik, P.H. Mayrhofer, H. Riedl, Phase formation and mechanical properties of reactively and non-reactively sputtered Ti–B–N hard coatings, *Surf Coat Technol* 420 (2021).
- [20] I. El Azhari, J. Garcia, M. Zamanzade, F. Soldera, C. Pauly, L. Llanes, F. Mücklich, Investigations on micro-mechanical properties of polycrystalline Ti(C,N) and Zr(C,N) coatings, *Acta Mater* 149 (2018) 364–376.
- [21] M. Tkadletz, N. Schalk, A. Lechner, L. Hatzenbichler, D. Holec, C. Hofer, M. Deluca, B. Sartory, A. Lyapin, J. Julin, C. Czettl, Influence of B content on microstructure, phase composition and mechanical properties of CVD Ti(B,N) coatings, *Materialia (Oxf)* 21 (2022).
- [22] Y.H. Lu, P. Sit, T.F. Hung, H. Chen, Z.F. Zhou, K.Y. Li, Y.G. Shen, Effects of B content on microstructure and mechanical properties of nanocomposite Ti–B[sub x]–N[sub y] thin films, *Journal of Vacuum Science & Technology B: Microelectronics and Nanometer Structures* 23 (2005) 449.
- [23] C. Kainz, N. Schalk, M. Tkadletz, C. Mitterer, C. Czettl, The effect of B and C addition on microstructure and mechanical properties of TiN hard coatings grown by chemical vapor deposition, *Thin Solid Films* 688 (2019).
- [24] A.B. Mei, H. Kindlund, E. Broitman, L. Hultman, I. Petrov, J.E. Greene, D. Sangiovanni, Adaptive hard and tough mechanical response in single-crystal B1 VN_x ceramics via control of anion vacancies, *Acta Mater* 192 (2020) 78–88.
- [25] P. Ström, D. Primetzhofer, Ion beam tools for nondestructive in-situ and in-operando composition analysis and modification of materials at the Tandem Laboratory in Uppsala, *Journal of Instrumentation* 17 (2022).
- [26] M. Janson, CONTES conversion of time-energy spectra—A program for ERDA data analysis, (2004).
- [27] R.M. Langford, M. Rogers, In situ lift-out: Steps to improve yield and a comparison with other FIB TEM sample preparation techniques, *Micron* 39 (2008) 1325–1330.
- [28] W.C. Oliver, G.M. Pharr, An improved technique for determining hardness and elastic modulus using load and displacement sensing indentation experiments, *J Mater Res* 7 (1992) 1564–1583.
- [29] A.C. Fischer-Cripps, Critical review of analysis and interpretation of nanoindentation test data, *Surf Coat Technol* 200 (2006) 4153–4165.
- [30] G.C.A.M. Janssen, M.M. Abdalla, F. van Keulen, B.R. Pujada, B. van Venrooy, Celebrating the 100th anniversary of the Stoney equation for film stress: Developments from polycrystalline steel strips to single crystal silicon wafers, *Thin Solid Films* 517 (2009) 1858–1867.
- [31] K. Matoy, H. Schönherr, T. Detzel, T. Schöberl, R. Pippan, C. Motz, G. Dehm, A comparative micro-cantilever study of the mechanical behavior of silicon based passivation films, *Thin Solid Films* 518 (2009) 247–256.
- [32] G. Kresse, J. Furthmüller, Efficient iterative schemes for ab initio total-energy calculations using a plane-wave basis set, *Phys Rev B* 54 (1996) 11169–11186.
- [33] G. Kresse, D. Joubert, From ultrasoft pseudopotentials to the projector augmented-wave method, *Phys Rev B* 59 (1999) 1758–1775.
- [34] W. Kohn, L.J. Sham, PHYSICAL REVIEW Self-Consistent Equations Including Exchange and Correlation Effects*, n.d. 2023.
- [35] J.P. Perdew, K. Burke, M. Ernzerhof, Generalized Gradient Approximation Made Simple, 1996.
- [36] D. Nöger, A command line tool written in Python/Cython for finding optimized SQS structures, (2019).
- [37] Y.Le Page, P. Saxe, Symmetry-general least-squares extraction of elastic data for strained materials from ab initio calculations of stress, *Phys Rev B Condens Matter Mater Phys* 65 (2002) 1–14.
- [38] R. Yu, J. Zhu, H.Q. Ye, Calculations of single-crystal elastic constants made simple, *Comput Phys Commun* 181 (2010) 671–675.
- [39] P. Lazar, J. Redinger, R. Podloucky, Density functional theory applied to VN/TiN multilayers, *Phys Rev B Condens Matter Mater Phys* 76 (2007).
- [40] M. Bielawski, K. Chen, Computational evaluation of adhesion and mechanical properties of nanolayered erosion-resistant coatings for gas turbines, *J Eng Gas Turbine Power* 133 (2011).
- [41] K. Xu, Y.L. Meng, S.M. Liu, J. Tan, Controllable Optical Characteristics of TiN Films Prepared by Magnetron Sputtering, in: *Lecture Notes in Electrical Engineering*, Springer Science and Business Media Deutschland GmbH, 2021: pp. 131–138.
- [42] D. Martínez-Martínez, C. López-Cartes, A. Fernández, J.C. Sánchez-López, Exploring the benefits of depositing hard TiN thin films by non-reactive magnetron sputtering, *Appl Surf Sci* (2013) 121–126.
- [43] P.H. Mayrhofer, F. Kunc, J. Musil, C. Mitterer, A comparative study on reactive and non-reactive unbalanced magnetron sputter deposition of TiN coatings, 2002.
- [44] L. Shizhi, S. Yulong, P. Hongrui, Ti–Si–N Films Prepared by Plasma-Enhanced Chemical Vapor Deposition, 1992.
- [45] S. Vepřek, S. Reiprich, L. Shizhi, Superhard nanocrystalline composite materials: The TiN/Si₃N₄ system, *Appl Phys Lett* (1995) 2640.
- [46] J. Patscheider, T. Zehnder, M. Diserens, Structure-performance relations in nanocomposite coatings, 2001.